Time-domain excitation of quantized magnetostatic spin-wave modes in patterned NiFe thin film ensembles

T. M. Crawford,* M. Covington, and G. J. Parker
Seagate Research, 1251 Waterfront Place, Pittsburgh, Pennsylvania 15222
(Received 18 June 2002; revised manuscript received 29 October 2002; published 16 January 2003)

We measure quantized spin waves excited by a spatially inhomogeneous pulsed magnetic field in patterned NiFe thin films by inductive detection of the dynamic magnetization. When anisotropy and numerically calculated demagnetizing fields are included in the magnetostatic Damon–Eshbach spin-wave dispersion relation, the predicted mode frequencies agree closely with measurements. Micromagnetic calculations predict the correct mode frequencies and agree remarkably well with time-domain measurements.

DOI: 10.1103/PhysRevB.67.024411 PACS number(s): 75.40.Gb, 75.30.Ds, 75.50.Ss, 76.50.+g

The rapid advance of magnetic data storage technology has driven groundbreaking work in the study of ferromagnetic materials at high frequencies. Measurements have been performed on patterned, multilayered devices, as well as new ferromagnetic materials and geometries.[1–4] In particular, laterally patterned ferromagnetic films have exhibited multiple resonances, arising from the excitation of quantized spin-wave modes.[5–8] These spin waves are termed magnetostatic spin waves or magnetostatic modes because the excitation wavelength is long compared with the sample exchange length.[9] These studies have built upon older experimental and theoretical work where spin-wave excitations were first studied experimentally in ferrites and ferromagnets.[9–12] The majority of these studies have been performed at large static magnetic field values ($>$100–200 Oe), and have employed small-excitation-signal techniques, such as Brillouin Light Scattering (BLS)[6] or ferromagnetic resonance (FMR).[5]

Patterned ferromagnetic thin films exhibit complex behavior. Even for simple materials and geometries, e.g., $Ni_{80}Fe_{20}$ (NiFe) rectangles, circles, etc., differing interpretations of similar data on spin wave properties may readily be found.[5,8,13,14] A complete understanding of the high frequency behavior in patterned NiFe is necessary if investigations are to be extended to new ferromagnetic materials and devices. To complete this understanding, measurements of spin wave modes in NiFe films could be extended to smaller static magnetic fields, $<$200 Oe, where magnetization nonuniformity could modify the spin-wave spectrum, and published results are scarce due to the large bias fields typically employed in BLS.[5] Comparative measurements could be performed in the time-domain, where fast rise-time magnetic field pulses force the system to respond to a simultaneous excitation by multiple frequencies.[1,4,15] In this case, multiple spin waves may co-exist temporally and spatially. Time-domain measurements typically employ larger pulsed field amplitudes than small-signal techniques, and previous observations have suggested that nonlinear coupling between spin-wave modes may occur at large pulsed fields.[4] We address these issues, by applying large amplitude, time-domain pulsed magnetic fields to patterned NiFe devices. Our pulsed fields are applied in a controlled, non-uniform spatial geometry, with static magnetic fields in the range from 0 to 150 Oe.

Our devices consist of coplanar microwave waveguides (CPW) designed for 50 Ω impedance, which overlay patterned NiFe thin film ensembles. Using an ensemble of elements increases signal-to-noise with inductive detection while measuring averaged single element dynamics. Our NiFe films have 50 and 100 nm thicknesses, and are deposited using dc magnetron sputtering onto substrates coated with amorphous Al_2O_3. The samples are then patterned into squares 50 μm on a side. Seventeen of these squares are arrayed in 1 mm ensembles, with easy axes parallel to the ensemble axis. A 0.94 μm Al_2O_3 spacer is deposited on the NiFe elements. Following the Al_2O_3 deposition, a 0.75 μm thick Cu film is deposited and patterned into CPWs with center conductor widths of 15 and 25 μm, ground plane widths of 31 and 52 μm, for total widths of 90 and 151 μm, respectively, and total lengths of $\sim$1 mm. The 15 μm CPW is centered with respect to the 50×50 μm^2 squares, while the 25 μm CPW is offset so the center conductor covers one-half of the 50×50 μm^2 ensemble. Figure 1 shows the in-plane field profile of the 15 μm waveguide, calculated using the Biot–Savart law,[16] along with a top-view of the

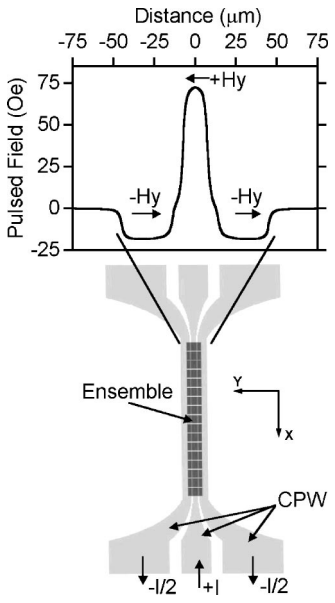

FIG. 1. Coplanar waveguide (CPW) and ensemble layout, along with calculated Biot–Savart fields for the 15 μm CPW in the tapered region as shown.

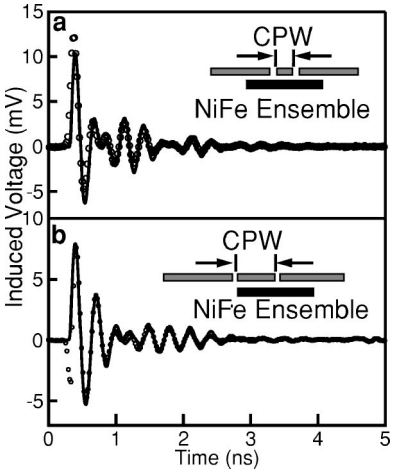

FIG. 2. Inductive voltage from an ensemble of 50×50 μm^2 elements, as a function of time (60 Oe static bias field). (a) Voltage response of a centered 15 μm CPW (7 Oe pulsed field); (b) response of an offset 25 μm CPW. The solid lines in (a)–(b) are 3D numerical micromagnetic calculations as described in the text.

waveguide/ensemble geometry. The magnetic field from the center conductor is directed along the $+y$ direction, while the field from the ground planes is directed along $-y$. The ground plane and center conductor currents are also indicated.

To detect the temporal magnetization response, we use an inductive technique.[4] A step current pulse, which has a 70 ps risetime and 20 ns duration, is transmitted through the CPW. A 70 Oe peak magnetic field can be generated along the *y*-axis by our largest pulse amplitude of 9 V, although we can attenuate this pulse to <7 Oe to vary pulsed field amplitude. The pulse drives the magnetization out of equilibrium, creating a voltage that propagates with the original pulse. Using a 18 GHz sampling oscilloscope, we perform 1024 averages at 100 kHz pulse repetition rate, while applying a static field of 150 Oe also along the *y*-axis (''saturation'' field). We then repeat the measurement with the static field directed along the *x*-axis, varying from 0 to 150 Oe (bias field). Finally, the two curves are subtracted to yield the inductive voltage created by the dynamic magnetization. Our case is different from previous time-domain inductive measurements,[4] because we measure the sum of voltages induced by the individual ensemble elements.

The time-domain behavior of our ensemble devices is shown in Figs. 2(a)–2(b), where we plot induced voltage as a function of time for the 15 and 25 μm CPW cases, respectively (100 nm film thickness), for a 7 Oe pulsed field (along the *y*-axis) and 60 Oe bias field. The cross sectional geometries for the two cases are shown as insets in Fig. 2. Both traces show a time-domain beating of multiple frequencies with similar amplitudes. Baseline measurements performed on an ensemble of 15×15 μm^2 squares and on a 1×1 mm^2 sample, both centered on a 15 μm CPW, exhibit single frequency response.

The time-domain response is well-fitted by two linearly-superposed, exponentially-damped sinusoids having nearly equal amplitudes but different frequencies.[4] As will be shown in detail below, this behavior arises from the excitation of a pair of the available quantized magnetostatic spin-wave eigenmodes of the 50 μm NiFe sample.

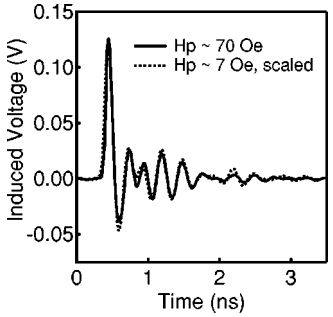

FIG. 3. Response comparing 70 Oe and 7 Oe pulsed fields (7 Oe data is scaled by $10\times$). Note the near perfect match between the curves, indicating that the induced voltage varies linearly with pulsed field amplitude.

Figure 3 shows the voltage from the 15 μm CPW (100 nm thickness, 60 Oe bias), for two pulsed field amplitudes: 70 Oe (solid line), and 7 Oe (dotted line, scaled by $10\times$). The curves agree closely, and a similar, linear scaling with pulsed field is observed over a wide range of bias fields. In contrast to previous time domain studies,[4] we find no evidence for nonlinearity at large pulsed fields.

Fourier transforming (FFT) the time domain responses from Figs. 2(a)–2(b), the rms amplitudes as a function of frequency are shown in Fig. 4(a). As in the time domain data, two dominant frequency modes are seen for both curves in Fig. 4(a). Comparing the solid and dashed curves, the peak separation is different for the two waveguide geometries. The lower frequency peaks agree within experimental error, while the higher frequency peaks are clearly different. We note that in previous studies of patterned NiFe typically more than two modes are observed.[6] In fact, measurements on an

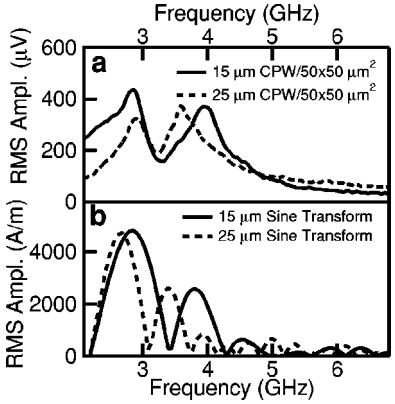

FIG. 4. Frequency response obtained via FFT of time domain data. (a) rms mode amplitude as a function of frequency for the two geometries in Figs. 2(a)–2(b). Note the overlap between the lower frequency peaks and the separation of the higher frequency peaks. (b) CPW spatial field amplitude as a function of frequency. The frequency axis is calculated from the spatial wave vector, using the dispersion relation in Eq. (3) for a continuous wave vector. Note the general agreement between the spatial frequency peaks and the dominant excited spin wave modes.

identical sample geometry with a 3 μm CPW center conductor, using a frequency-resolved optical technique, detect five quantized modes.[17] These results suggest that the spatially inhomogeneous field from the CPW (Fig. 1 top) excites a sub-set of the available quantized spin-wave eigenmodes, as previously observed in ferrite spheres.[10]

To further understand the nature of these spin-wave modes, we perform 3D numerical micromagnetic calculations of the ensemble's temporal response. This response is calculated using the Landau–Lifshitz equation,

$$d\mathbf{m}/dt = -\frac{\gamma}{1+\alpha^2}\mathbf{m}\times[\mathbf{H}+\alpha\mathbf{m}\times\mathbf{H}], \qquad (1)$$

where $\mathbf{m}=\mathbf{M}/M_s$ is the unit magnetization vector, M_s is the (assumed constant) saturation magnetization, t is time, γ is the gyromagnetic ratio, α is the phenomenological Gilbert damping coefficient, and $\mathbf{H}$, in the magnetostatic limit, is given by:

$$\mathbf{H} = -\nabla\Phi + \frac{2A}{M_s}\nabla^2\mathbf{m} + \frac{2K}{M_s}(\mathbf{m}\cdot\mathbf{c})\mathbf{c} + \mathbf{H}_b + \mathbf{H}_p, \qquad (2)$$

where the first term is the magnetostatic field ($\nabla^2\Phi = 4\pi M_s\nabla\cdot\mathbf{m}$), $A=1.6\times10^{-11}$ J/m is the exchange constant, K is the magnetocrystalline anisotropic constant, $\mathbf{c}$ is the uniaxial anisotropy direction, and the remaining terms are the Zeeman fields for the uniform biasing (along x) and nonuniform excitation (along y and z), respectively. In our calculations, the magnetization domain is discretized uniformly along each Cartesian axis, thereby allowing efficient fast Fourier transforms for the volumed averaged magnetostatic field for each computational cell, and a simple 7-point Laplacian stencil for the exchange field. The volume averaged excitation field, $\mathbf{H}_p$, for each computational cell is found analytically from the Biot–Savart Law given the geometry of the CPW, spacing from the magnetic elements (0.94 μm), and assuming an infinite CPW along the bias field (x-axis) and a spatially uniform current in the thin CPW with temporal behavior determined by experimental observations. Equation (1) is solved semi-implicitly with a fixed time step of 0.1 ps. There are no explicit boundary conditions on the magnetization profile since the calculation correctly incorporates all the relevant physics; e.g., the magnetostatic (and, to a lesser extent, exchange) fields naturally ''pin'' the magnetization along the element surfaces for the geometries considered here. Due to computational feasability, the 3D simulations reported here have computational cells larger than the exchange length. However, finer meshing in 3D, along with simulations in 2D where the exchange length scale can be resolved, show no effect on the final computed results and also confirm that the spin waves are purely magnetostatic in nature. In the 3D simulations, all of the ensemble elements are assumed to have identical magnetic response.

The magnetization-induced voltage is calculated by reciprocity in the standard formalism.[4] In particular, a fictitious current is passed through the CPW. The resulting field in the magnetic sample is projected along the instantaneous magnetization profile and volume integrated. The (numerical) time derivative of this volume integrated projection is then proportional to the induced voltage. The solid lines in Figs. 2(a)–2(b) are the micromagnetically calculated voltage responses for the two cases shown, using $\gamma/2\pi = 32.2$ GHz/T, $4\pi M_s = 1.05$ T, $H_k \equiv 2K/M_s = 4$ Oe, and $\alpha = 0.01$. This value of $4\pi M_s$ is accurate within 5%–10% for our NiFe films. The y component of $\mathbf{H}_p$ has the profile shown in Fig. 1. We note that this value of α is consistent with that found for much larger samples.[18] The calculated voltages agree closely with the measured ones, indicating that our calculation successfully captures the relevant physics underlying these spin-wave excitations.

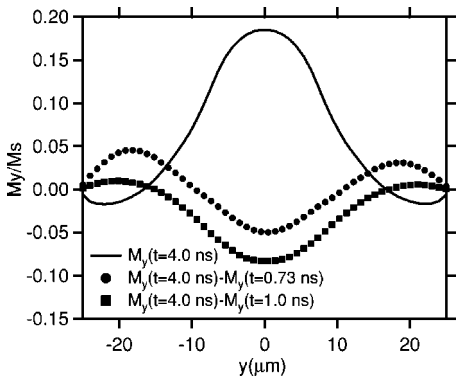

FIG. 5. Micromagnetically simulated spatial magnetization response: magnitude of M_y as a function of y. The steady state M_y configuration for $t=4.0$ ns is given as the solid line. The difference between the steady state M_y and M_y at $t=0.73$ ns after the step excitation is given by the circles, while the squares denote the difference in M_y between $t=4.0$ ns and $t=1.0$ ns. Note that M_y is pinned at the sample edges and consists of two dominant spatial frequencies, which can be seen in the deviations of M_y from its steady state configuration. For these curves, every fifth computational point has been plotted, where the first and last points give M_y closest to the sample edges.

Figure 5 shows the y-component of the magnetization for the simulations shown in Fig. 2(a). The steady state M_y configuration after the step excitation is given as the solid line. The deviation of M_y from this configuration is shown at two instances of time after the step excitation, $t=0.73$ ns and $t=1.0$ ns, as circles and squares, respectively. These deviations in M_y clearly show the two normal modes which are simultaneously excited. The simulations in Fig. 5 show M_y going to zero at the sample edges, indicating that M_y is pinned, as discussed above. Figure 6 shows FFT's of the simulated time domain voltages for the data from Fig. 2(a) for three different current/field configurations. The solid line is for the case shown in Fig. 1. The dashed line is for the case where the field is only that of the center conductor, and the ground plane fields (i.e., currents) are set equal to zero. The dotted line is for the case where the field above the ground planes is equal to that above the CPW center conductor. In all three cases, only two modes are observed, and their frequencies are independent of ground plane field strength. However, the relative amplitudes of the modes strongly depends on the relative fields from the ground planes. The agreement between experiment and simulation, as shown in

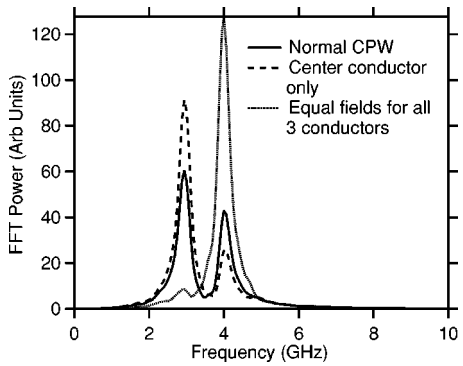

FIG. 6. FFT's of simulated time domain voltages for different waveguide field configurations for the 15 μm waveguide geometry. Solid line: FFT of simulated time-domain response for field profile shown in Fig. 1. Dashed line: FFT for the case where the ground plane fields are zero and only the field above the center conductor is present. Dotted line: FFT for the case where the fields above the ground planes are equal to the field above the center conductor. All three cases show two modes with identical frequencies. However, the magnitudes of the peaks strongly depend on the relative fields in the ground planes and center conductor, implying that a correct treatment of both center conductor and ground planes is required to obtain the agreement between experiment and simulation shown in Figs. 2(a)–2(b).

Fig. 2, cannot be obtained without including the correct ground plane fields. Further, measurements of the 25 μm offset sample for waveguides without a ground plane over the sample confirm the change in mode amplitude that is predicted by the FFT's in Fig. 6.

As mentioned above, interpretations of spin wave properties differ in the literature for similar patterned NiFe film structures. We now analyze our data from Fig. 2, to address these differences. Figure 7 displays spin-wave frequency squared, f^2, as a function of bias field, for the 15 and 25 μm CPW devices [Fig. 7(a)], and for 15 μm CPWs at two film thicknesses: 50 and 100 nm [Fig. 7(b)]. A linear dependence

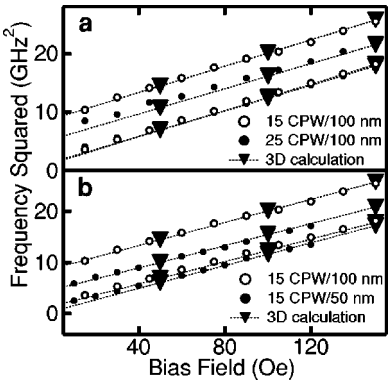

FIG. 7. Spin wave mode frequencies, squared, as a function of bias field. (a) Comparison of mode frequencies for 15 μm ($n=1,3$) and 25 μm ($n=1,2$) CPWs. (b) comparison of 15 μm CPW frequencies ($n=1,3$) for 50 and 100 nm thick films. The inverted triangles are 3D micromagnetic calculations. The dotted lines connecting the calculated frequencies are not fitted, but touch most of the experimental points.

of f^2 on bias field is expected from the Damon–Eshbach (DE) dispersion relation for magnetostatic spin waves (see below).[11,13] The squared frequencies in Fig. 7 appear approximately linear vs bias field over the full field range ($\sim$15–150 Oe). The inverted triangles in Fig. 7 are calculated via micromagnetics for $H_b=50$, 100, and 150 Oe, and, as in Fig. 2, the calculated f^2 are in excellent agreement with experiment. The lines in Fig. 7 are drawn through the calculated points to show the agreement with experiment, and are not fitted. Having reproduced our experimental results numerically, to make quantitative predictions, we compare our frequencies with those predicted by the DE dispersion relation:[11,13]

$$f^2=\left(\frac{\gamma}{2\pi}\right)^2[4\pi M_s H_b+(2\pi M_s)^2(1-\exp(-2\pi ns/w))]$$
$$\equiv\left(\frac{\gamma}{2\pi}\right)^2 4\pi M_s[H_b+H_n]\equiv\left(\frac{\gamma}{2\pi}\right)^2 4\pi M_s\mathcal{H}', \qquad (3)$$

for standing wave modes quantized along y, where n is the integer mode index, w is the width of the sample, and s is the thickness. For ease of comparison with experiment, we calculate $\mathcal{H}'$ from the frequencies in Fig. 7, inserting the same values of γ and $4\pi M_s$ used for the numerical calculations. Given the discussion above, we apply Eq. (3) with pinned boundary conditions, i.e., our mode indices start with $n=1$ (the lowest unpinned mode has $n=0$).[5] However, the experimental $\mathcal{H}'$, from Fig. 7, are lower than the predicted $\mathcal{H}'$. Equation (3) predicts $\mathcal{H}'=92.8$ Oe ($H_{n=1}=32.8$ Oe; $H_b=60$ Oe; $w=50$ μm; $s=100$ nm). For the lowest frequency mode in Fig. 7(a) ($n=1$), $\mathcal{H}'=78.9\pm3$ Oe. For $H_b=150$ Oe, Eq. (3) predicts $\mathcal{H}'=182.8$ Oe, while Fig. 7(a) yields $\mathcal{H}'=167\pm8$ Oe (uncertainties assume 5% error in $4\pi M_s$). Similar disagreement occurs if one takes $n=0$. The decreased sensitivity of the measurement at the higher bias fields highlights the importance of being able to perform these measurements at bias fields well below 100 Oe. Previous studies have shown similar discrepancies, which are resolved either by using unpinned boundary conditions or non-integer mode-indices,[5,8,13] both of which lower the predicted $\mathcal{H}'$. However, as written, Eq. (3) does not include uniaxial anisotropy or demagnetizing field anisotropy, both of which are present in our case. We modify Eq. (3) to include these terms:

$$f^2=\left(\frac{\gamma}{2\pi}\right)^2[4\pi M_s(\mathcal{H}'+H_d+H_k)]=\left(\frac{\gamma}{2\pi}\right)^2 4\pi M_s\mathcal{H} \qquad (4)$$

where H_d is the demagnetizing field along the CPW axis and will be negative since it opposes H_b inside the sample. The uniaxial anisotropy field, $H_k=2K/M_s=4$ Oe, is measured prior to film patterning with a M-H looper. H_d is calculated numerically, by computing the volume-averaged internal field at a given H_b. We again combine these terms and define the sum as $\mathcal{H}$. Using Eq. (4) with numerically derived $H_d=-18.4$ Oe along with $H_{n=1}$ and H_k, we calculate $\mathcal{H}=78.4$ Oe ($H_b=60$ Oe), compared with $\mathcal{H}=78.9\pm3$ Oe from Fig. 7. The micromagnetically calculated $\mathcal{H}$

$=77.1$ Oe. The predicted $\mathcal{H}$ agrees closely with the $\mathcal{H}$ from both experiment and micromagnetics. Similar agreement is obtained for all the modes in Figs. 7(a)–7(b). For the third mode in Fig. 7(a) ($n=3$), we derive $\mathcal{H}=144.9\pm6$ Oe ($H_b=60$ Oe), while numerically, $\mathcal{H}=146.8$ Oe, and Eq. (4) predicts $\mathcal{H}=142.7$ Oe. Equation (3) would have predicted $\mathcal{H}'=157$ Oe for this case. By including H_k and H_d in our analysis, we obtain excellent agreement with DE dispersion, with pinned boundary conditions and integer mode indices.

To further establish the validity of Eq. (4), we performed the same measurement shown in Fig. 2 on a 50 μm wide (y) by 1000 μm long (x) rectangle, using an identical 15 μm CPW. Under these conditions, H_d in Eq. (4) should be negligible in comparison to the 50×50 μm^2 case. We find $\mathcal{H}=97\pm4$ Oe for the lower mode ($H_b=60$ Oe). Substituting $H_{n=1}=32.8$ Oe, $H_k=4.0$ Oe, and $H_d=0$ into Eq. (4), we predict $\mathcal{H}=96.8$ Oe, again in excellent agreement with experiment. As a further check, the micromagnetic calculated response of an ensemble of 50 μm wide (y) by 25 μm long (x) elements found only an offset in both mode frequencies, suggesting that Eq. (4) properly accounts for the demagnetizing field. We also computed the case where the frequency difference is not independent of the boundary conditions, by making film thickness, s, a bigger fraction of sample width, w. The simulated frequency difference requires the lowest two modes to have indices $n=1$ and $n=2$, not $n=0$ and $n=1$, i.e., largely pinned boundaries (for even larger s/w values, neither ''pinned'' nor ''unpinned'' are correct).

To explain in detail how the CPW field profiles lead to the observed spin-wave spectra, we examine the pulsed field spatial harmonics seen by the sample. Assuming mostly pinned boundary conditions for the magnetization at the lateral edges ($y=\pm25$ μm), we expand the fields from the CPW using only sine terms in the Fourier expansion.[19] Two dominant peaks are seen in the spatial frequency spectra for the two CPWs, as shown in Fig. 4(b), where the solid and dashed lines are for the 15 and 25 μm CPWs, respectively. These spatial frequency spectra mirror the observed spin wave spectra shown in Fig. 4(a). To make this comparison more quantitative, the x-axis in Fig. 4(b) was computed by transformation of wave vector to frequency via the dispersion relation [Eq. (3)]. The spatial harmonics shown in Fig. 4(b) overlap the measured frequencies in Fig. 4(a), for both the 15 and 25 μm CPWs, indicating that we can both predict and control which of the spin wave modes will be excited for a given field geometry. To test whether this spatially selective excitation depends on the detection geometry, we micromagnetically calculated the effect of varying CPW width and placement for the inductive detection only (excitation geometry was held constant). The results showed no shifts in peak frequency nor any additional spectral peaks, suggesting that our induced voltage correctly represents the excited magnetization.

In conclusion, we demonstrate the ability to spatially control the excited spin-wave spectrum in a patterned ferromagnetic thin film. We successfully employ 3D micromagnetic calculations to reproduce our measured voltages in the time domain, and no nonlinearities are observed, even at large pulsed fields. We obtain close agreement between measured and predicted absolute frequency and frequency separation, using the Damon–Eshbach dispersion relation, modified to include uniaxial anisotropy and demagnetizing fields, with pinned boundary conditions.

The authors wish to acknowledge Adnan Rebei, Jim Bain, Shingo Tamaru, and Rene van de Veerdonk for useful discussions and helpful insight.

*Electronic address: thomas.m.crawford@seagate.com

[1] B. C. Choi, M. Belov, W. K. Hiebert, G. E. Ballentine, M. R. Freeman, Phys. Rev. Lett. **86**, 728 (2001).
[2] Y. Acremann *et al.*, Science **290**, 492 (2000).
[3] J. F. Smyth *et al.*, J. Appl. Phys. **69**, 5262 (1991).
[4] T. J. Silva, C. S. Lee, T. M. Crawford, and C. T. Rogers, J. Appl. Phys. **85**, 7849 (1999).
[5] P. H. Bryant, J. F. Smyth, S. Schultz, and D. R. Fredkin, Phys. Rev. B **47**, 11 255 (1993).
[6] C. Mathieu *et al.*, Phys. Rev. Lett. **81**, 3968 (1998).
[7] C. Mathieu *et al.*, Appl. Phys. Lett. **75**, 3859 (1999).
[8] Y. Roussigne, S. M. Cherif, C. Dugautier, and P. Moch, Phys. Rev. B **63**, 134429 (2001).
[9] L. R. Walker, Phys. Rev. **105**, 390 (1957).
[10] R. L. White, I. H. Solt, Phys. Rev. **104**, 56 (1956).
[11] R. W. Damon and J. R. Eshbach, J. Phys. Chem. Solids **19**, 308 (1961).
[12] C. E. Patton, Phys. Rep. **103**, 251 (1984).
[13] J. Jorzick *et al.*, Phys. Rev. B **60**, 15 194 (1999).
[14] K. Y. Guslienko, S. O. Demokritov, B. Hillebrands, and A. N. Slavin, Phys. Rev. B **66**, 132402 (2002).
[15] T. M. Crawford, P. Kabos, and T. J. Silva, Appl. Phys. Lett. **76**, 2113 (2000).
[16] J. D. Jackson, *Classical Electrodynamics*, 3rd ed. (Wiley, New York, 1999).
[17] S. Tamaru, J. A. Bain, R. J. M. van de Veerdonk, T. M. Crawford, M. Covington, and M. H. Kryder, J. Appl. Phys. **91**, 8034 (2002).
[18] M. Covington, T. M. Crawford, and G. J. Parker, Phys. Rev. Lett. **89**, 237202 (2002).
[19] W. H. Press, B. P. Flannery, S. A. Teukolsky, and W. T. Vetterling, *Numerical Recipes in C* (Cambridge University Press, Cambridge, 1988) p. 418.